Small-scale structure of the Kane oceanic core complex, Mid-Atlantic Ridge 23°30′N, from waveform tomography of multichannel seismic data

J. Pablo Canales[1]

Received 21 June 2010; revised 20 August 2010; accepted 27 August 2010; published 3 November 2010.

[1] Frequency-domain waveform tomography applied to deep-sea multichannel seismic data collected across the Kane oceanic core complex (OCC) reveals the small-scale structure of this section of oceanic lithosphere formed at the Mid-Atlantic Ridge 3.3–2.1 Myr ago that has been uplifted and exhumed at the seafloor along an oceanic detachment fault. Geological and geophysical studies indicate that the central-eastern area of the Kane OCC is formed by a large gabbroic intrusion. The new high-resolution seismic velocity models show that this gabbroic core is 1,000–1,350 m thick and it is underlain by a ~300-m-thick layer of low-velocity material interpreted as serpentinized peridotite. The models also reveal the presence of a deeper, 200-m-thick by 1,700-m-long high-velocity body interpreted as a small gabbroic sill embedded in serpentinzed peridotite. **Citation:** Canales, J. P. (2010), Small-scale structure of the Kane oceanic core complex, Mid-Atlantic Ridge 23°30′N, from waveform tomography of multichannel seismic data, *Geophys. Res. Lett.*, *37*, L21305, doi:10.1029/2010GL044412.

1. Introduction

[2] Oceanic lithosphere formed along slow- and ultra-slow spreading centers is compositionally and structurally heterogeneous at many different scales due to temporal and spatial variations in mantle composition and thermal structure, magma supply, efficiency of melt extraction, tectonic extension, or a combination of any of these factors [e.g., *Cannat et al.*, 1995; *Dick et al.*, 2003; *Hooft et al.*, 2000]. This compositional and structural variability is exposed in oceanic core complexes (OCCs), which are sections of the oceanic lithosphere exhumed to the seafloor by long-lived detachment faults formed along the flanks of mid-ocean ridges [e.g., *Cann et al.*, 1997; *MacLeod et al.*, 2002; *Tucholke et al.*, 1998].

[3] Active-source wide-angle seismic methods are commonly used to infer the large-scale seismic properties of the oceanic lithosphere [e.g., *Hooft et al.*, 2000]. However their resolving power is often limited by several factors, such as poor spatial sampling and the use of the ray approximation in travel time tomography (TT) inversions. Waveform tomography (WT) methods that minimize the full waveform residual (as opposed to simply the travel time of a particular seismic phase) have the potential to produce results that are manifestly superior than those obtained from TT methods, and at greater resolving power close to the seismic wavelength of the targets [e.g., *Brenders and Pratt*, 2007]. Results from WT studies using synthetic, noise-free datasets [e.g., *Brenders and Pratt*, 2007] indicate that WT, if applied to suitable real datasets, should be capable of imaging the structure of slow-spreading lithosphere at scales comparable of those of seafloor geological observations and deep-drilling borehole measurements. However its application in marine seismology remains largely unexploited because of computational requirements and lack of adequate datasets; only a handful of studies using ocean bottom seismometer or multichannel seismic (MCS) reflection datasets have been published to date [*Dessa et al.*, 2004; *Hicks and Pratt*, 2001; *Operto et al.*, 2006; *Shipp and Singh*, 2002].

[4] Here I choose the method of *Pratt* [1999], based on a finite-difference solution of the acoustic-wave equation in the frequency-wavenumber domain, to assess the potential and limitations of applying WT to deep-sea MCS data acquired in complex, unsedimented tectonic settings. In this paper I present results from applying frequency-domain WT to data collected at the Kane OCC off the Mid-Atlantic Ridge (MAR), where the lithological variability of the exposed lithosphere is well documented.

2. Kane Oceanic Core Complex

[5] The Kane OCC, presently located between ~30 and 55 km west of the MAR spreading axis (Figure 1), formed between 3.3 Ma and 2.1 Ma with a half spreading rate of 15 mm/yr [*Williams et al.*, 2006]. The exposed detachment fault constituting the surface of the OCC exhibits several domes and is cut by a large-offset, high-angle, west-facing normal fault (East Fault, Figure 1). Extensive geological sampling indicates that the central and western parts of the Kane OCC are predominantly ultramafic, while both peridotites and gabbros are exposed along the northern edge of the OCC [e.g., *Dick et al.*, 2008]. Slide scars along the East Fault expose massive outcrops of serpentinized peridotite at the center of the OCC, providing direct evidence of the footwall composition there [*Dick et al.*, 2008].

[6] *Canales et al.* [2008] used MCS data collected across the Kane OCC (Figure 1) to derive TT seismic velocity models of the shallow lithosphere (<2 km sub-seafloor depth) exhumed by the detachment fault (Figure 2). These models show an excellent correlation between seafloor geology and subsurface seismic structure, revealing the large-scale lithological heterogeneity of the OCC. Areas with high velocities near the seafloor (>4.2 km/s) were interpreted as large gabbro plutons and are mostly present beneath the Babel Dome and eastern half of the Cain Dome. Intermediate shallow velocities (3.4–4.2 km/s) were

[1]Woods Hole Oceanographic Institution, Woods Hole, Massachusetts, USA.

Copyright 2010 by the American Geophysical Union.
0094-8276/10/2010GL044412

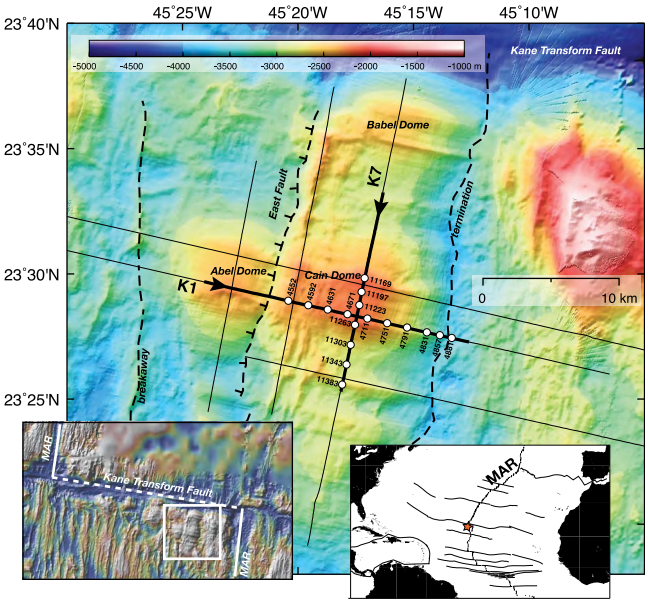

Figure 1. Bathymetry of the Kane OCC (insets show its geographical location). Thin lines are the EW0102 MCS profiles; bold lines correspond to the sections of profiles K1 and K7 modeled in this study. Numbered open circles are some of the shot locations. Arrowheads indicate the direction of shooting. Simplified geological features and nomenclature are from *Dick et al.* [2008].

interpreted as serpentinized peridotite, dominating the central (Abel Dome and western half of Cain Dome) and south-eastern parts of the OCC. Areas with low shallow velocities (<3.4 km/s) corresponded to regions of extrusive volcanics.

3. Results From Frequency-Domain Waveform Tomography

3.1. Acquisition Geometry and Data Processing

[7] Data used in this study were acquired in 2001 onboard *R/V M. Ewing* (cruise EW0102) using a 6-km-long streamer with 480 hydrophone groups spaced every 12.5 m. The sound source was a 10-air-gun array (total volume of 51 L) triggered every 37.5 m. For this study I selected a subset of data covering two sections from profiles K1 and K7 (Figure 1). One out of every second shot was selected, resulting in a source spacing of 75 m. This choice ensures that, for sub-seafloor velocities greater than 3 km/s, the wavefield in the receiver domain is spatially unaliased for frequencies lower than 20 Hz [e.g., *Bleibinhaus et al.*, 2009]. Data processing consisted of muting and interpolating noisy traces, applying surface-consistent amplitude balancing, and band-pass filtering (3–5–20–30 Hz).

[8] Prior to the inversion the shot gathers were windowed in the time-offset domain after applying a velocity reduction of 2 km/s and selecting a time window of 0–1.8 s in the 160 far-offset traces (4,182–6,182 m source-receiver offsets, Figure 3a). Due to seafloor depth variations, only a small fraction of shot gathers contain significant refracted energy at offsets smaller than 4,000 within this reduced-time window; thus the choice of 4,182 m as a minimum usable offset. However this choice has some negative impacts for the inversion: it narrows the range of wavenumbers for which amplitude variations with offset contribute to the data residuals, and limits the model resolution at the shallowest levels. However the windowing allows excluding energy from seafloor reflections and scattering. These water-wave arrivals have significantly higher amplitude than any sub-seafloor arrival and would dominate the data residuals of the inversion.

3.2. Model Setup

[9] *P*-wave velocity, density, and attenuation models were defined in regular grids with 12.5 m node spacing (1601-by-401 nodes for K1, 1201-by-321 nodes for K7), extending from sea level to 6 km depth. The models include accurate sea floor topography based on multibeam bathymetry data collected along the seismic profiles. The starting velocity models were the TT models of *Canales et al.* [2008] (Figures 2a and 2c). Density models were derived from the *P*-wave velocity models assuming the density-velocity relationship of *Carlson and Raskin* [1984]. Attenuation was set to a constant value of $Q_P^{-1} = 10^{-4}$ for the water layer (where Q_P is the quality factor for *P* waves), and $Q_P^{-1} = 10^{-3}$ for the rest of the model to simulate a low attenuation medium. This choice was justified by comparing the RMS of amplitudes versus offset behavior of sub-seafloor arrivals between the data and the synthetic seismograms predicted by the TT velocity model.

3.3. Inversion Strategy

[10] I followed a two-stage, multiscale full WT strategy similar to that described by *Brenders and Pratt* [2007] and *Bleibinhaus et al.* [2009] by simultaneously inverting at each stage a group of a few frequency components of the data, progressing from low to high frequencies (Table 1). The starting models for stage 2 were the resulting models of the previous stage. Prior to each inversion the source wavelet was estimated from the data using the starting velocity model [*Pratt*, 1999] (Figure 3e). During each stage, the gradient of the misfit function [*Pratt*, 1999] was pre-conditioned by allowing perturbations to the gradient only between the seafloor and 4 km depth, tapering off at 4.5 km depth, and filtering the gradient in the wavenumber domain (Table 1).

[11] The amplitude spectrum of the data (Figure 3d) is poor in frequencies lower than 15 Hz and has several amplitude lows (notches) at key frequencies (e.g., 10 and 20 Hz), probably because of a poorly tuned airgun array. Attempts were made to start the inversion with lower frequency components of the data (i.e., the 7–10 Hz peak, Figure 3d); however the results were unsatisfactory due to high-velocity artifacts in the resulting velocity model. Another possible cause preventing successful inversions of the lower frequencies is the data window selected. The windowed signal after the first arrival within the ~4,000–4,500 m offset range might be too short to extract information from the lower frequencies (Figure 3a). For this reason I focused on inverting the range of frequencies between 13 and 19 Hz, which includes the maximum amplitude of the spectrum at 15 Hz and has the largest signal-to-noise ratio (Figure 3d). For the range of shots considered in this study, the starting model fits the travel time of first arrivals with a RMS misfit of 14 ms [*Canales et al.*, 2008], which corresponds to about a quarter of the period of a 16 Hz signal. This ensures that inversion artifacts due to cycle skipping [*Pratt*, 1999] are avoided even when

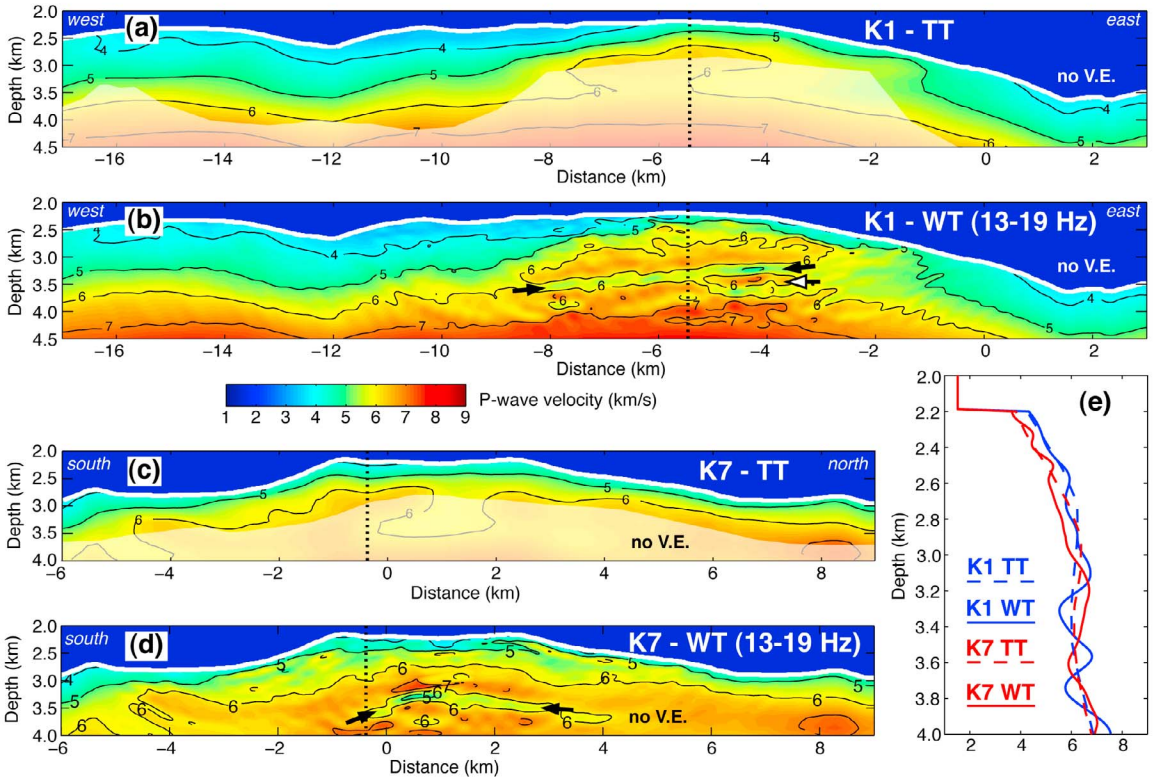

Figure 2. *P*-wave velocity models for profiles (a, b) K1 and (c, d) K7. Models in Figures 2a and 2c correspond to the TT results of *Canales et al.* [2008]; masked areas are regions without ray coverage. Models in Figures 2b and 2d correspond to the final WT results. Contours labeled in km/s. Thick white line is the seafloor. Black arrows in Figures 2b and 2d highlight a thin low velocity channel. White arrow in Figure 2b points to a small high velocity lens. All images are shown with no vertical exaggeration. (e) Velocity-depth functions extracted from the TT (dashed lines) and WT results (solid lines) at the intersection between profiles K1 and K7 (dashed lines in Figures 2a–2d).

the low frequency components of the data are not included in the inversion.

3.4. Data Fit

[12] The goodness of the fit between the observed and the predicted waveforms is given by the misfit function E, which includes the amplitude and phase data residuals. The reduction in E is surprisingly small (2–9%, Table 1). One of the reasons for this is that the decrease in data residuals after each iteration occurs primarily in the phase component of the residuals, with less improvement taking place in the amplitude component. This was tested by conducting inversions in which the amplitude of the observed and predicted data were normalized, resulting in a misfit function that only takes into account phase data residuals. The phase-only inversions reduce the misfit function by a larger amount (12–26%), but the resulting velocity models are not very different from those obtained from the amplitude +phase inversions. In contrast to other studies in which noisy amplitudes deteriorate results [e.g., *Bleibinhaus et al.*, 2009], the stable inversion of phases and amplitudes could be due to the high signal-to-noise ratio for the range of frequencies considered, the absence of near surface and sensor coupling issues, and/or the consistency of both source signature and receiver response. Therefore I choose to present and discuss here the results from the phase +amplitude inversions.

[13] The validity of the final velocity models can be qualitative assessed by comparing the data with synthetic gathers predicted by the TT and the final WT velocity models. Figure 3b shows an example of a synthetic gather for profile K1 in which a secondary, diffracted arrival predicted by the TT model is consistent with the data (white arrows in Figures 3a and 3b), but also includes arrivals that are not clearly seen in the data (gray arrow in Figure 3b). The WT synthetic gather (Figure 3c) shows a clear improvement in the match between observed and predicted secondary arrivals. Some arrivals present in the data but not predicted by the TT model are now well predicted by the WT model (black arrows in Figures 3a and 3c); and those arrivals wrongly predicted by the TT model (gray arrow in Figure 3b) are absent in the WT synthetic gather.

[14] Figure S1 of the auxiliary material presents more examples of data from profile K1 compared to synthetic seismograms in which the improved match between arrivals in the observed and WT synthetic gathers is highlighted.[1] Despite the small decrease in misfit function obtained during the inversions and the non-uniqueness of the inversions, the clear improvement in the characteristics of the WT synthetic shot gathers with respect to those predicted by the TT model

[1] Auxiliary materials are available in the HTML. doi:10.1029/2010GL044412.

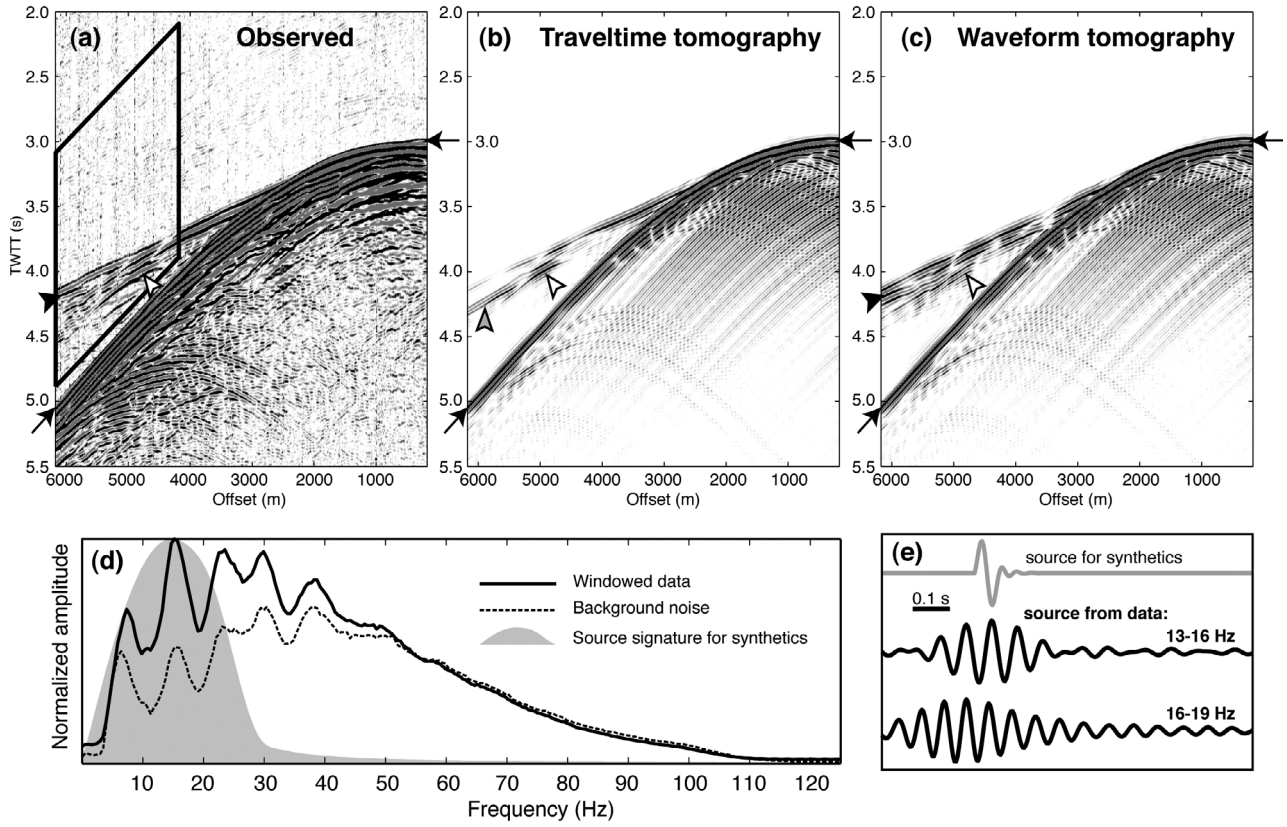

Figure 3. (a) Shot gather 4735 from profile K1. Black trapezoid corresponds to the data window for WT. (b, c) Synthetic shot gathers predicted by the TT and WT velocity model (Figures 2a and 2b), respectively. Synthetic seismograms were calculated using a finite-difference solution of the acoustic-wave equation in the frequency domain [*Pratt and Worthington*, 1990] for 360 frequencies evenly spaced between 0 and 30 Hz. Arrowheads in Figures 3a–3c point to arrivals in the data that are well predicted by the TT and WT models (white), arrivals predicted by the TT model but that are not observed in the data (gray), and arrivals not predicted by the TT model but observed in the data and well predicted by the WT model (black). Arrows point to the seafloor reflection. (d) Amplitude spectrum of the windowed data used in the inversions (solid), background noise (dashed), and of the source wavelet used to calculate the synthetics seismograms (shaded). (e) Source wavelets used to calculate the synthetics seismograms (gray) and estimated from the data for each frequency group used in the inversions (solid).

indicates that the WT results are realistic, and provides confidence when interpreting them.

3.5. Interpretation

[15] There is a clear increase in the level of detail of the final WT velocity models when compared to the TT models, particularly at the center of the profiles (Figure 2). Most of the model update occurs at depths below the first-arrival ray coverage predicted by the TT models (Figure 2) because the data includes many secondary arrivals such as those highlighted in Figures 3 and S1.

[16] The most significant feature observed in the WT model of K1 is a ~300-m-thick low velocity channel with velocities of 5.4–5.6 km/s embedded within a 6.4–6.7 km/s matrix (Figure 2b). This channel dips gently towards the west at sub-seafloor depths ranging from 1,000 m near $X = -3.2$km, to 1,250 m near $X = -8.4$ km. Figure S2 includes a test showing the amplitude variations in the observed data that constrain the presence of this feature.

[17] A similar feature is observed at profile K7 between $X = 4.0$ km $X = -0.4$ km at depths of 1,050–1,350 m below the seafloor (Figure 2d). However this low velocity channel along profile K7 does not extend farther south than the intersection with profile K1, and it is located 300 m deeper in K7 than in K1 at the intersection between both profiles (Figure 2e). Possible reasons for this discrepancy include anisotropy, 3D topography effects and energy scattering at the steepest parts of the seafloor (e.g., southern flank of Cain Dome, $X = [-3, -1]$ km in profile K7) that produce amplitude variations in the seismograms that cannot be fully accounted for with the method used.

Table 1. Inversions Parameters[a]

			K1		K7	
Frequencies (Hz)	k_x^{-1} (m)	k_z^{-1} (m)	ΔE (%)	N	ΔE (%)	N
13, 14, 15, 16	372	186	4	8	9	7
16, 17, 18, 19	313	157	2	9	9	8

[a] k_x and k_z are the cutoff horizontal and vertical wavenumbers, respectively, used for low-pass filtering of the gradient of the misfit function. ΔE is the reduction in misfit function, and N is the number of iterations.

[18] The relatively fast velocities found in the TT models of *Canales et al.* [2008] at shallow levels across the eastern half of Cain Dome (profile K1, $X = [-8, -3]$ km) and from the southern end of Cain dome to Babel Dome (profile K7, $X = [-5, 9]$ km) were interpreted by these authors as a large gabbro pluton(s). However, the TT models could not resolve the thickness of such gabbro bodies. The low velocity channel imaged by the WT models can be interpreted as the bottom boundary of the shallow large gabbro body forming eastern half of the Cain Dome. Velocities within the channel are too low to represent unaltered/unfractured gabbro [e.g., *Miller and Christensen*, 1997]. A possible interpretation would be that the low velocity channel is a thin layer of highly altered and fractured (at seismic wavelengths) gabbro; however it is difficult to envision a tectonic mechanism that would create such channel without fracturing and/or altering the material above it. More likely the low velocity channel corresponds to a layer of highly serpentinized peridotite. This would indicate that the large gabbro pluton was intruded into mantle rock, consistent with the hypothesis that oceanic detachment faults may develop at the rheological boundary formed around the margins of gabbro plutons intruded in peridotite [*Ildefonse et al.*, 2007].

[19] The gabbro pluton may have been intruded in an already hydrated part of the mantle; or alternatively, formation of the serpentine channel may have followed the intrusion of gabbro as the heat released from the intrusion drives hydrothermal circulation within the peridotite matrix, forming a serpentine sheath around the margins of the pluton. Also, the nature of the material beneath the low velocity channel (less altered mantle or a deeper gabbro body) remains unconstrained because model updates between 4.0 and 4.5 km depth were damped during the inversions; thus results are very dependent on the starting velocity model, which at those depths was not constrained by turning rays (Figure 2a).

[20] Another feature observed in the WT model of K1 is a ~200-m-thick, ~1,700-m-long high velocity (6.0–7.2 km/s) lens centered near $X = -4.2$ km at ~1,200 m below the seafloor (Figure 2b), surrounded by low velocities (5.0–5.5 km/s). This feature is interpreted as a small gabbroic sill embedded in serpentinized peridotite. The geological significance of this feature within the broader picture of the formation of the Kane OCC is probably small. However its importance resides in that it demonstrates that the resolution of WT is far superior to that of TT, and that WT can image targets at scales close to the seismic wavelength. A resolution test (Figure S3) demonstrates that this feature is required by the data.

4. Conclusions

[21] 1. Despite the limitations of the method and dataset employed, the results presented here demonstrate that frequency-domain WT methods can image the structure of oceanic lithosphere at scales that were not possible with conventional TT methods.

[22] 2. High-resolution seismic velocity models of the Kane OCC show that the high-velocity gabbroic core forming the eastern side of the Cain Dome is 1,000–1,350 m thick and it is underlain by a thin (300 m) channel of low-velocity material interpreted as serpentinized peridotite. The WT images also reveal the presence of a deeper, 200-m-thick by 1,700-m-long high-velocity body interpreted as a small gabbroic sill embedded in serpentinzed peridotite.

[23] **Acknowledgments.** The author thanks the *Andrew W. Mellon Foundation Endowed Fund for Innovative Research* for the award that supported this study, the WHOI Deep Ocean Exploration Institute for travel funds to participate in the 2005 Short Course on Waveform Tomography organized by G. Pratt and A. Brenders, S.C. Singh and M.R. Nedimović for discussions during the early stages of this study, and S. Nag (2007 WHOI Summer Student Fellow) for implementing in the source code the use of a variable seafloor interface to define the non-varying part of the model. Reviews by J. Hole and an anonymous reviewer helped improved the quality of the manuscript.

References

Bleibinhaus, F., R. W. Lester, and J. A. Hole (2009), Applying waveform inversion to wide-angle seismic surveys, *Tectonophysics*, *472*(1–4), 238–248, doi:10.1016/j.tecto.2008.08.023.

Brenders, A. J., and R. G. Pratt (2007), Full waveform tomography for lithospheric imaging: Results from a blind test in a realistic crustal model, *Geophys. J. Int.*, *168*, 133–151, doi:10.1111/j.1365-246X.2006.03156.x.

Canales, J. P., B. E. Tucholke, M. Xu, J. A. Collins, and D. L. DuBois (2008), Seismic evidence for large-scale compositional heterogeneity of oceanic core complexes, *Geochem. Geophys. Geosyst.*, *9*, Q08002, doi:10.1029/2008GC002009.

Cann, J. R., D. K. Blackman, D. K. Smith, E. McAllister, B. Janssen, S. Mello, E. Avgerinos, A. R. Pascoe, and J. Escartín (1997), Corrugated slip surfaces formed at ridge-transform intersections on the Mid-Atlantic Ridge, *Nature*, *385*, 329–332, doi:10.1038/385329a0.

Cannat, M., et al. (1995), Thin crust, ultramafic exposures, and rugged faulting patterns at the Mid-Atlantic Ridge (22°–24°N), *Geology*, *23*, 49–52, doi:10.1130/0091-7613(1995)023<0049:TCUEAR>2.3.CO;2.

Carlson, R. L., and G. S. Raskin (1984), Density of the ocean crust, *Nature*, *311*, 555–558, doi:10.1038/311555a0.

Dessa, J.-X., S. Operto, S. Kodaira, A. Nakanishi, G. Pascal, J. Virieux, and Y. Kaneda (2004), Multiscale seismic imaging of the eastern Nankai trough by full waveform inversion, *Geophys. Res. Lett.*, *31*, L18606, doi:10.1029/2004GL020453.

Dick, H. J. B., J. Lin, and H. Schouten (2003), An ultraslow-spreading class of ocean ridge, *Nature*, *426*, 405–412, doi:10.1038/nature02128.

Dick, H. J. B., M. A. Tivey, and B. E. Tucholke (2008), Plutonic foundation of a slow-spreading ridge segment: Oceanic core complex at Kane Megamullion, 23°30′N, 45°20′W, *Geochem. Geophys. Geosyst.*, *9*, Q05014, doi:10.1029/2007GC001645.

Hicks, G. J., and R. G. Pratt (2001), Reflection waveform inversion using local descent methods: Estimating attenuation and velocity over a gas-sand deposit, *Geophysics*, *66*(2), 598–612, doi:10.1190/1.1444951.

Hooft, E. E. E., R. S. Detrick, D. R. Toomey, J. A. Collins, and J. Lin (2000), Crustal and upper mantle structure along three contrasting spreading segments of the Mid-Atlantic Ridge, 33.5°–35°N, *J. Geophys. Res.*, *105*, 8205–8226, doi:10.1029/1999JB900442.

Ildefonse, B., D. K. Blackman, B. E. John, Y. Ohara, D. J. Miller, C. J. MacLeod, and I. O. E. S. Party (2007), Oceanic core complexes and crustal accretion at slow-spreading ridges, *Geology*, *35*(7), 623–626, doi:10.1130/G23531A.1.

MacLeod, C. J., et al. (2002), Direct geological evidence for oceanic detachment faulting: the Mid-Atlantic Ridge, 15°45′N, *Geology*, *30*(10), 879–882, doi:10.1130/0091-7613(2002)030<0879:DGEFOD>2.0.CO;2.

Miller, D. J., and N. I. Christensen (1997), Seismic velocities of lower crustal and upper mantle rocks from the slow spreading Mid-Atlantic Ridge, south of the Kane transform zone (MARK), *Proc. Ocean Drill. Program Sci. Results*, *153*, 437–454.

Operto, S., J. Virieux, J.-X. Dessa, and G. Pascal (2006), Crustal seismic imaging from multifold ocean bottom seismometer data by frequency domain full waveform tomography: Application to the eastern Nankai trough, *J. Geophys. Res.*, *111*, B09306, doi:10.1029/2005JB003835.

Pratt, R. G. (1999), Seismic waveform inversion in the frequency domain, part 1: Theory and verification in a physical scale model, *Geophysics*, *64*(3), 888–901, doi:10.1190/1.1444597.

Pratt, R. G., and M. H. Worthington (1990), Inverse theory applied to multi-source cross-hole tomography. Part 1: Acoustic wave-equation method, *Geophys. Prospect.*, *38*, 287–310, doi:10.1111/j.1365-2478.1990.tb01846.x.

Shipp, R. M., and S. C. Singh (2002), Two-dimensional full wavefield inversion of wide-aperture marine seismic streamer data, *Geophys. J. Int.*, *151*, 325–344, doi:10.1046/j.1365-246X.2002.01645.x.

Tucholke, B. E., J. Lin, and M. C. Kleinrock (1998), Megamullions and mullion structure defining oceanic metamorphic core complexes on the Mid-Atlantic Ridge, *J. Geophys. Res.*, *103*, 9857–9866, doi:10.1029/98JB00167.

Williams, C. M., M. A. Tivey, and M. D. Behn (2006), The magnetic structure of Kane megamullion: Results from marine magnetic anomalies, paleomagnetic data and thermal modeling, *Eos Trans. AGU*, *87*(52), Fall Meet. Suppl., Abstract T42A-03.

J. P. Canales, Woods Hole Oceanographic Institution, MS 24, 360 Woods Hole Rd., Woods Hole, MA 02543, USA. (jpcanales@whoi.edu)